Intermittency at Earth's bow shock: Measures of turbulence in quasi-parallel and quasi-perpendicular shocks

James Plank[1] and Imogen Gingell[2]

[1]University of Southampton
[2]Imperial College London

November 26, 2022

Abstract

Recent simulations and observations have revealed reconnecting current sheets in the turbulent transition region of Earth's bow shock. However, the link between reconnection in the shock and turbulent reconnection in the magnetosheath is unknown. We have therefore used observations from Magnetospheric Multiscale (MMS) over four separate bow shock crossings of varying ϑ_Bn to characterise turbulence in the shock transition region and how it evolves towards the magnetosheath. We fit power laws to the magnetic spectrum over many short intervals, allowing us to observe the spectrum evolving. We find that we can separate the behaviour of the power-law index in the shock transition region from that of the upstream and downstream plasma when ϑ_Bn is in the quasi-perpendicular range (45º

Intermittency at Earth's bow shock: Measures of turbulence in quasi-parallel and quasi-perpendicular shocks

J. Plank[1], I. L. Gingell[1]

[1]School of Physics & Astronomy, University of Southampton, Southampton, UK

Key Points:

- We examine the evolution of turbulent fluctuations across Earth's bow shock using magnetic spectra, kurtosis and correlation length.
- The power-law magnetic spectra in the shock transition region are found to be distinct from the solar wind and magnetosheath.
- The correlation length of high-pass filtered fluctuations shows fast reduction of the driving scale across a quasi-perpendicular shock.

Corresponding author: James Plank, `jp5g16@soton.ac.uk`

Abstract

Recent simulations and observations have revealed reconnecting current sheets in the turbulent transition region of Earth's bow shock. However, the link between reconnection in the shock and turbulent reconnection in the magnetosheath is unknown. We have therefore used observations from Magnetospheric Multiscale (MMS) over four separate bow shock crossings of varying θ_{Bn} to characterise turbulence in the shock transition region and how it evolves towards the magnetosheath. We fit power laws to the magnetic spectrum over many short intervals, allowing us to observe the spectrum evolving. We find that we can separate the behaviour of the power-law index in the shock transition region from that of the upstream and downstream plasma when θ_{Bn} is in the quasi-perpendicular range ($45^\circ < \theta_{Bn}$) but not when θ_{Bn} is quasi-parallel ($\theta_{Bn} < 45^\circ$). Across the shock, we also see a distinct change in the breakpoint location between inertial and ion power-law slopes. We also observe the evolution of scale-independent kurtosis of magnetic fluctuations across the shock, finding that 72.4% of the upstream interval in a quasi-perpendicular shock exhibits a kurtosis > 3 versus 23.1% downstream, compared to a quasi-parallel shock where we see 22.8% upstream and 17.0% downstream. This relationship is more apparent in the quasi-perpendicular case. Finally, we adapt a method for calculating correlation length to include a high-pass filter, allowing us to obtain estimates for changes in correlation length across Earth's bow shock corrected for the positive bias introduced by large scale shock structures. We find that correlation lengths are a factor of at least 10 smaller in the magnetosheath than in solar wind in a quasi-perpendicular shock but do not vary significantly in an extended quasi-parallel shock with a significant amount of foreshock activity. Upstream structures in both quasi-perpendicular and quasi-parallel shocks can reduce correlation length for short periods of time (10s of seconds).

Plain Language Summary

Turbulence is a phenomenon that can arise in anything that behaves like a fluid under certain conditions. The size and shape of turbulent vortices and eddies can tell us a lot about the energy contained within the fluid. For example, highly energetic particles emitted from the Sun form a turbulent, fluid-like plasma called the solar wind. The Earth's magnetic field acts as an obstacle to the solar wind, forming a shock wave called the bow shock, similar to the shock wave formed by a supersonic jet in air. This shock wave is very complex and introduces an additional source of turbulent structures. In this paper, we looked at the turbulence just before the shock wave, during, and after to learn if its presence fundamentally changes how the energy gets distributed inside a turbulent plasma. We found evidence that turbulence behaves differently in these three areas. In addition, the magnetic field angle relative to the shock wave (i.e. nearly parallel/perpendicular to the shock) also has an effect.

1 Introduction

Turbulence is a ubiquitous phenomenon in space plasmas, occurring in systems ranging from star formation (McKee & Ostriker, 2007) to galaxy clusters (Zhuravleva et al., 2014) to planetary magnetospheres (Chasapis et al., 2018) and the solar wind (Alexandrova et al., 2013; Bruno & Carbone, 2013; Kiyani et al., 2015). In collisionless plasmas such as the solar wind, the mechanisms for dissipating energy in turbulence are not well-known (Kiyani et al., 2015), and solving this problem is vital for our understanding of turbulence in general. In the heliosphere, for example, turbulent dissipation is a suggested source of the heating observed in the Solar corona (Cranmer et al., 2015; Klimchuk, 2006). One of several proposed solutions to this dissipation problem is magnetic reconnection (Carbone et al., 1990; Franci et al., 2017), for which local changes in magnetic topology rapidly transfer energy from fields to particles, resulting in particle acceleration and heating (Burch et al., 2016). Some other possible explanations for energy dissipation include wave-particle interactions, driven by cyclotron resonance or kinetic Alfvén waves (Isenberg & Hollweg, 1983; Hollweg, 1999).

One advantage of using the local space environment to study plasma turbulence is that it allows for high-cadence in-situ observation of structures associated with turbulent dissipation, such as reconnecting current sheets. The Magnetospheric Multiscale (MMS) mission has recently been used to observe electron outflow jets at thin current sheets - a signature of reconnection - in Earth's magnetosheath (Phan et al., 2018) and the bow shock transition region (Gingell et al., 2019; Wang et al., 2017). Recent simulations (Bessho et al., 2020, 2022; Gingell et al., 2017; Matsumoto et al., 2015) have shown that processes in the shock foot can generate current sheets and magnetic islands, contributing to the formation of a transition region that can appear turbulent. The properties of turbulence are also known to vary across different plasma regimes, such as the solar wind and magnetosheath (Alexandrova, 2008). Furthermore, the properties of turbulence are also known to vary within the magnetosheath, varying with the upstream shock orientation (Yordanova et al., 2020) and between the sub-solar point and flanks (Huang et al., 2017; Sahraoui et al., 2020). This paper aims to address a significant open question when discussing turbulence at the bow shock: Can we measure a difference between turbulence seen in the bow shock transition region and in the surrounding plasma (i.e. the solar wind or magnetosheath)?

We note that some definitions of turbulence require a 'well-developed' inertial range, allowing a complete cascade from the largest, fluid-like scales in the plasma, through the kinetic regime and ending at the dissipation scale. In the shock transition region, apparently turbulent or disordered fluctuations may be driven by non-linear interactions and instabilities that arise below the inertial range, but nevertheless appear to cascade and dissipate energy in the region. For the purposes of this study, we will refer to these processes as turbulent, but acknowledge that they may not be fully developed.

In this paper, we study the evolution of magnetic fluctuations from the solar wind to magnetosheath, i.e. across the bow shock, using three different measures of turbulence: the magnetic spectrum, the kurtosis, and the correlation length (e.g. Stawarz et al., 2019). From the magnetic spectrum we extract the spectral break between inertial and ion scale ranges, which is related to local plasma scales such as the ion gyroradius ρ_i, and inertial length d_i (Chen et al., 2014; Franci et al., 2015). We also observe an increase in kurtosis immediately upstream of a quasi-perpendicular shock that is not observed in a quasi-parallel case. Finally, we use an adapted method of calculating correlation length to measure the local stirring scale of the turbulence, and find that the correlation length becomes several orders of magnitude smaller when moving from the solar wind to magnetosphere.

2 Data Set

We explore the bow shock transition using in situ data obtained by the Magnetospheric Multiscale (MMS) mission (Burch et al., 2015). Magnetic field data are provided by the fluxgate magnetometer (FGM) (Russell et al., 2014) and search coil magnetometer (SCM) (Contel et al., 2014). FGM and SCM data are analysed as a merged data set (FSM) (Argall et al., 2018). Particle data are provided by the Fast Plasma Investigation's (FPI) (Pollock et al., 2016) Dual Electron Spectrometer (DES) and Dual Ion Spectrometer (DIS). In high-resolution burst mode, the SCM magnetic fields are available at a sampling frequency of $F_s = 1/8192$ s, and the particle moments are available at a cadence of 0.15 s and 0.03 s for ions and electrons, respectively.

Four high-resolution (burst) bow shock crossing intervals have been analysed here. The events were chosen to cover a range of bow shock angles from quasi-perpendicular to quasi-parallel, where the burst interval was longer than approximately 10 minutes and

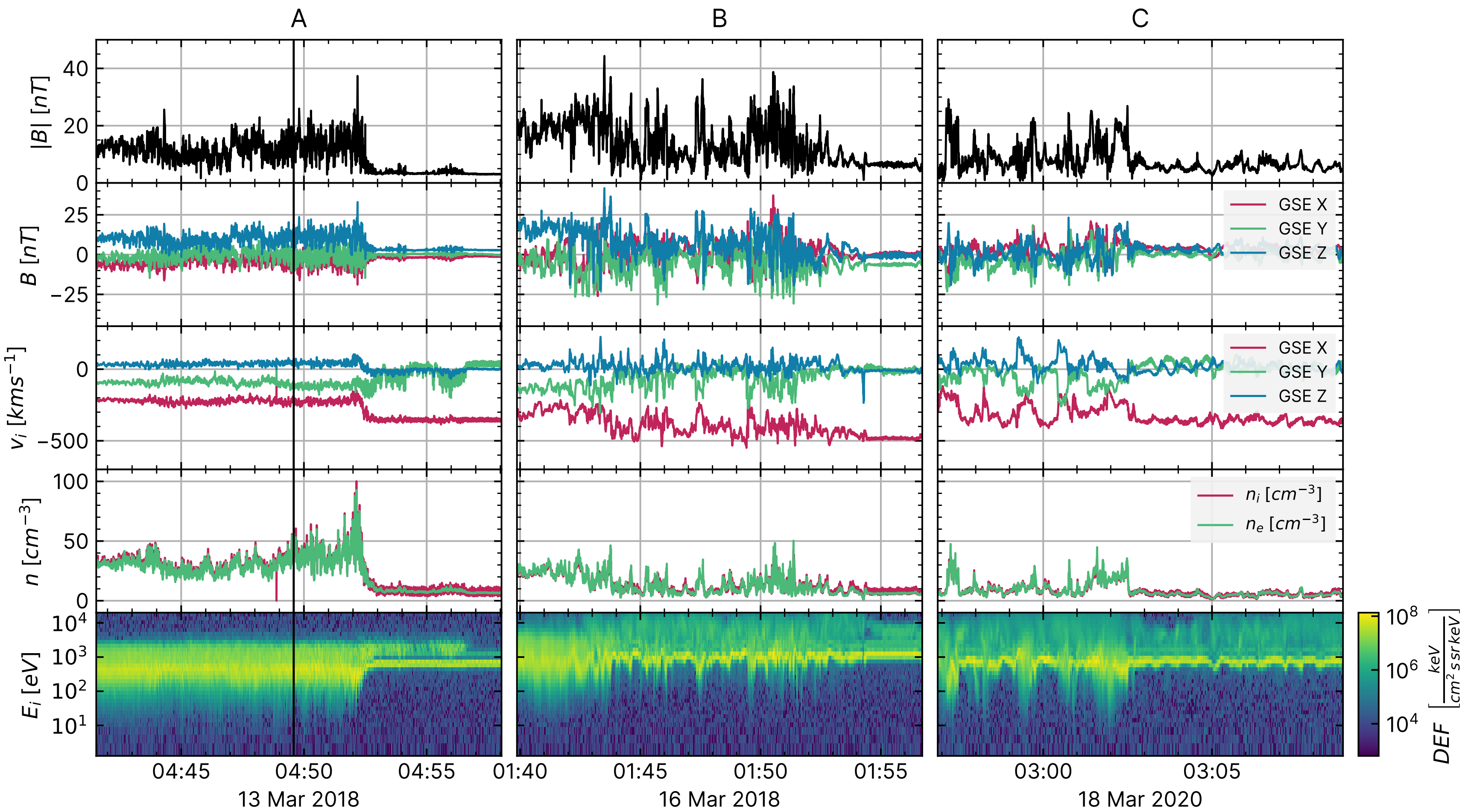

Figure 1. MMS observations showing events A (*left column*), B (*centre column*) and C (*right column*). *Row 1:* Magnetic field strength, $|\mathbf{B}|$; *Row 2:* Magnetic field components, $\boldsymbol{B}$, in GSE coordinates; *Row 3:* Ion velocity components, v_i (GSE); *Row 4:* Proton and electron densities, $n_{i,e}$; *Row 5:* Ion energy spectrogram. In each of the three cases, MMS crosses the shock from the magnetosheath side into the solar wind. The shock normal angles are $\theta_{Bn} = 68°$, $41°$, $35°$ from left to right respectively. The timestamp of Figure 3 is indicated by a vertical black line in the left column.

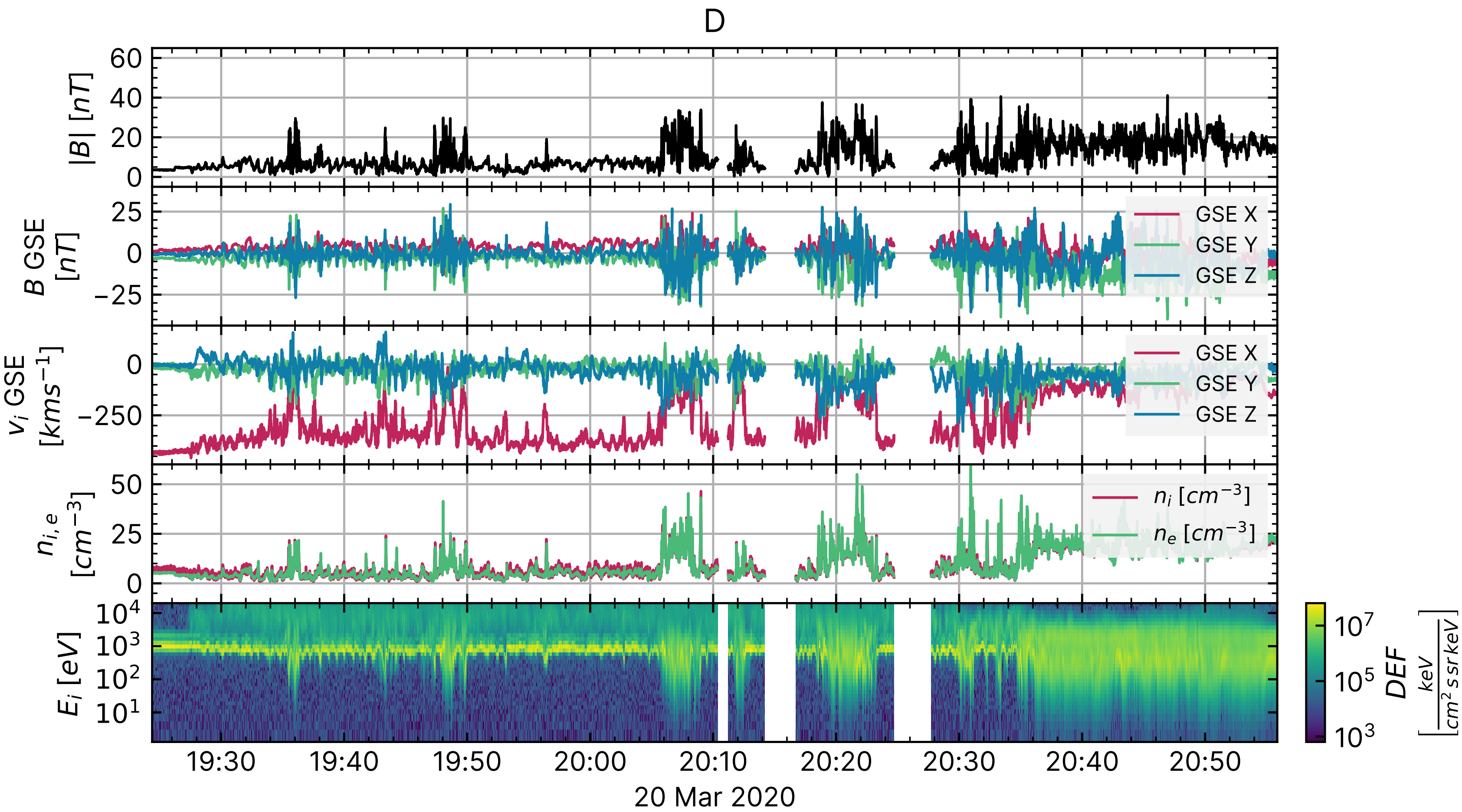

Figure 2. MMS observation of event D, lasting 226 minutes. Rows are the same as Fig.1. The shock normal angle is $\theta_{Bn} = 17°$. For this shock, MMS moves from the solar wind into the shock. There are three small gaps in the data starting at 20:10 and ending at 20:30. These gaps sum to less than 6 minutes in total.

where the shock was as close to the centre of the burst interval as possible, i.e. an ideal event would contain a roughly equal amount of solar wind and magnetosheath data. Figures 1 and 2 provide a summary of each of the events. The intervals on 13 March 2018, 16 March 2018, 18 March 2020 and 20 March 2020 are referred to as intervals A, B, C and D respectively. Events A-C are $\sim$ 15 minutes in duration, while event D is 226 minutes. Table 1 shows plasma parameters averaged over the entire interval, including electron upstream flow speed v_0, the acute angle between upstream magnetic field, $\mathbf{B}$, and the shock normal, θ_{Bn}, Alfvén Mach number M_A of the upstream flows, and the ion plasma beta β_i. The derived parameters M_A and β_i, along with observed values for v_0 and the magnetic field, were obtained from OMNI (King, 2005). The shock angle θ_{Bn} was calculated using a model from Peredo et al. (1995), using the upstream magnetic field lagged to the bow shock from OMNI and FPI moments from MMS.

The angle between the upstream magnetic field and shock normal angle, θ_{Bn}, decreases from quasi-perpendicular (68°) in event A to quasi-parallel (17°) in event D. Quasi-perpendicular shocks are characterised by near discontinuous transitions from the solar wind to bow shock. In contrast, a quasi-parallel shock has a more gradual transition and can often be complicated by upstream waves and instabilities caused by backstreaming ions in the foreshock. Therefore, the expectation is that structures created by the shock are more distinct in quasi-perpendicular shock crossings but are only observed for a short time, whereas a quasi-parallel shock will display a more complex behaviour that is challenging to separate from the solar wind or magnetosheath.

Table 1. Average upstream plasma properties as observed by OMNI and MMS. Data from OMNI were averaged over the same duration as MMS.

Interval	$\theta_{Bn}[°]$	$v_0[kms^{-1}]$	M_A	β_i	Start yyyy/mm/dd hh:mm:ss	End
A	68	356.4 ± 1.0	14.6 ± 1.1	4.4 ± 0.7	2018/03/13 04:41:33	04:58:02
B	41	475.8 ± 4.7	9.0 ± 0.7	1.4 ± 0.3	2018/03/16 01:39:53	01:56:43
C	35	394.4 ± 3.9	9.8 ± 0.8	2.2 ± 0.5	2020/03/18 02:56:53	03:08:52
D	17	405.0 ± 13.8	12.5 ± 0.7	3.0 ± 0.6	2020/03/20 19:24:23	20:55:52

3 The Magnetic Spectrum

In order to examine the evolution of the magnetic spectrum, events A-C were split into consecutive, non-overlapping windows containing 9 seconds of data per window. Event D was split into 45s windows to maintain visual clarity over the much longer event. There are 109, 112, 79 and 97 windows for each event A-D, resulting in $N \approx 7 \times 10^4$ or 4×10^5 field measurements per window for 9 or 45s windows respectively. The power spectrum of $\boldsymbol{B}$ in the spacecraft frame is given as, $PSD(\boldsymbol{B}, k)$, where $k = 2\pi f/v_0$, v_0 is the bulk flow speed and f is a discrete frequency increment in the range $N/f_s \leq f \leq f_s/2$. The transformation of frequency f to wavenumber k is performed assuming Taylor's hypothesis, which broadly states that any spacecraft motion is negligible when compared to the motion of the surrounding plasma, thus allowing us to use the spacecraft time series to explore the spatial domain. We calculate the trace power spectrum of the magnetic field, where components $B_{x,y,z}$ are pre-filtered with a Hanning window.

In a turbulent plasma, the magnetic spectrum often appears as a series of power laws with different indices, $P \propto k^\alpha$ (Frisch, 1995). For example, power-law index $\alpha = -5/3$ corresponds to the inertial range of fluid turbulence (Kolmogorov, 1941), typical of space plasmas at scales far above ion kinetic scales. At the ion scales, $\sim d_i$ or $\sim \rho_i$, solar wind and magnetosheath plasmas typically exhibit a breakpoint below which the magnetic spectrum steepens. In this ion kinetic range, the power-law index α is variable, though $\alpha \approx -2.8$ is typical for the solar wind (Alexandrova et al., 2009; Sahraoui et al., 2010). The breakpoint between the fluid MHD scale and the ion kinetic scale is at the larger of d_i, or ρ_i (Chen et al., 2014) when observing solar wind undisturbed by the bow shock. A second breakpoint is often observed at electron kinetic scales, and again the slope of the magnetic spectrum is expected to steepen in the electron kinetic range, below $\sim d_e$. Hence, the magnetic spectrum is expected to comprise three or more distinct power laws with different slopes. In order to characterise the power laws of our observed magnetic spectra, we seek an algorithm that can generate and fit an arbitrary number of straight lines to a spectrum, with a variable number of breakpoints. Hence, we use the Multivariate Adaptive Regression Splines (MARS) algorithm, developed by (Friedman, 1991), and implemented by (Milborrow et al., 2011).

Figure 3 shows an example of a spectrum obtained from an interval when MMS was downstream of the shock during event A, with the resultant MARS fit overlaid. Although we might expect the breakpoint between the inertial and ion kinetic ranges to be located at the larger of d_i or ρ_i, we instead observe that this breakpoint occurs at scales smaller than ρ_i. This may be due to the influence of the structure and waves associated with the bow shock, or it may be due to differences in turbulence properties in the magnetosheath when compared to the solar wind. We also note that an electron scale wave is visible at $k \approx 2\,\mathrm{km}^{-1}$ as a peak in the spectrum. Similar structures appear intermittently in all four intervals and are characterised by a dramatic change from positive to negative power law index at the electron scale.

Figures 4 and 5 show the evolution of spectral index with time for the intervals A and D, respectively. Equivalent plots are given for events B and C in the supplemental material, Figures S1 and S2. Each 9 or 45 second window is represented as a vertical slice where the index at a given scale corresponds to the MARS fit and consists of multiple bars coloured to represent the slope of the magnetic spectrum, spanning the range of scales (k) observable by MMS over the window duration.

We see that in the solar wind immediately preceding the shock, the breakpoint between the inertial (MHD) range and the ion (kinetic) range is much less than both d_i and ρ_i. This observation differs from studies, e.g. Chen et al. (2014), who suggest that in undisturbed solar wind, the spectral break should be d_i or greater. However, in the magnetosheath close to the shock, we find that the breakpoint shifts to larger scales and settles in the expected range $d_i \leq BP \leq \rho_i$.

Figure 6 shows the average slope as a function of scale, k, for intervals A and D, broken down into subsections based on MMS's location in relation to the shock, e.g. downstream (DS), in the shock transition region (STR), or the solar wind/foreshock (SW/FS). The chosen intervals corresponding to each region are shown in Figures 4, 5 for intervals A and D respectively. Similar figures for intervals B and C are given in the supplemental material, Figures S3 and S4. Errors shown are sample standard deviations from all windows within the region. The intuitive expectation is for the slope in the STR to be between those in the SW and DS at all scales. That is, we may expect to see the blue line (slope in the STR) to be between the green (DS) and yellow (SW) lines at all scales, as this would indicate that it is purely a transitional state as solar wind plasma crosses the shock and into the magnetosheath. However, we see that at multiple scales, the slope in the STR appears to be steeper than both SW and DS plasma, as in the case of electron-scale $k \approx 10^0 km^{-1}$, or shallower, as for the ion scales at $k \approx 10^{-2} km^{-1}$. The steepening of the spectra in the transition region at $k \approx 10^0 km^{-1}$ occurs at close to the electron-scales. This suggests that an electron-scale process is able to more efficiently dissipate energy from electron-scale fluctuations in this region, compared to the adjacent solar wind and magnetosheath.

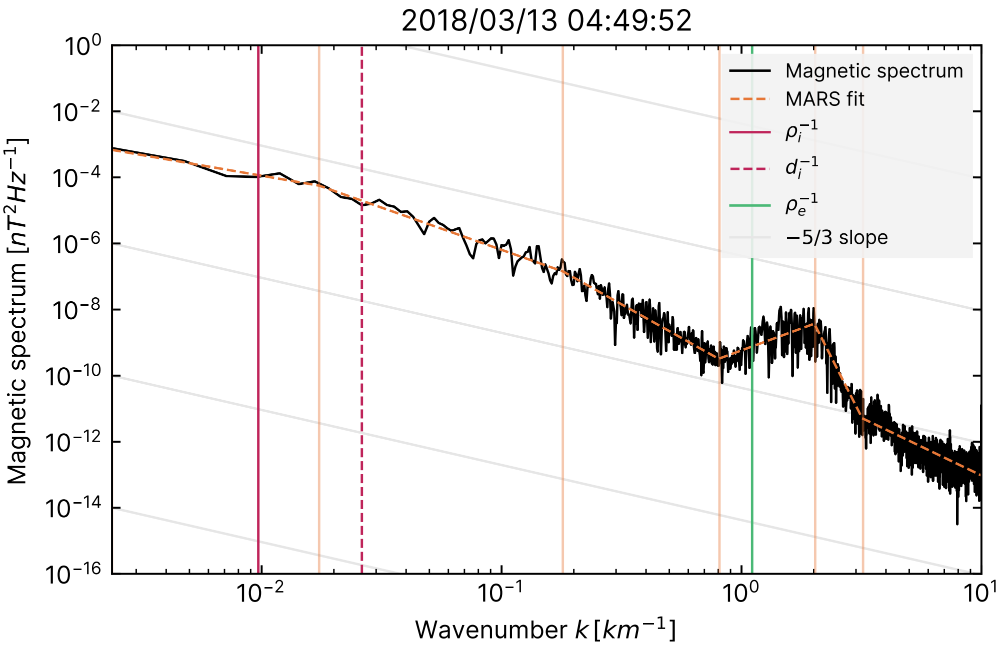

Figure 3. A plot of magnetic spectrum for an example ~ 6 s window downstream of the shock on 13/03/2018, illustrated as a vertical black line on Figure 1. Grid lines are shown with a slope of $-5/3$. The magnetic spectrum is shown in black. The ion and electron limits (ρ_i and $d_{i,e}$) are shown as red and green vertical lines. The fit to the spectrum is shown as an orange dashed line, built from chained linear regressions using the MARS method. Vertical orange lines highlight breakpoints determined by the MARS fit. An electron scale wave is visible at approximately $k \approx 2/\rho_e$, and this is reflected in the MARS fit by steep upward and downward slopes.

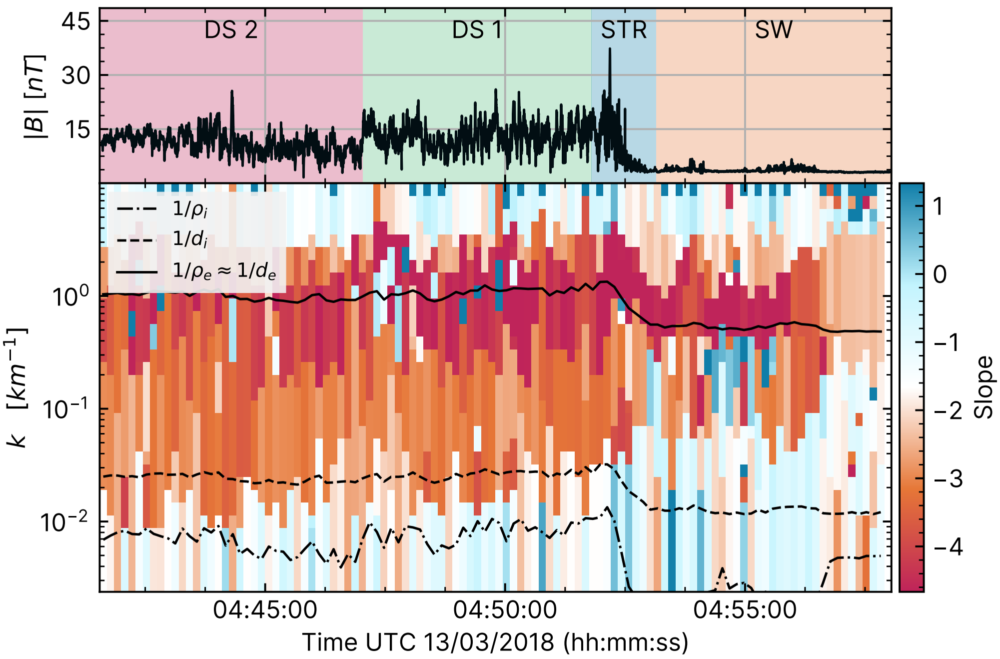

Figure 4. Evolution of spectral slopes as a function of time for event A. *Top:* Magnetic field strength, $|\boldsymbol{B}|$. Colours refer to downstream (DS 1/2), shock transition region (STR) and solar wind (SW) *Bottom:* Evolution of spectral indices from MARS fit. Note that this does not always split the spectrum into three regions. The colour represents the slope of the power-law fit. Red indicates steeper than $-5/3$, while blue is shallower than $-5/3$. Breakpoints are indicated by a change in colour. Electron scales, $\rho_e \approx d_e$ are shown as a solid black line, and ion scales d_i and ρ_i are dashed and dot-dashed black lines. Event A is a quasi-perpendicular shock and as a result we get a clear distinction between solar wind and magnetosheath spectra. The ion-inertial breakpoint (BP) is $<< d_i$ in the solar wind and rapidly transitions to $d_i < BP \leq \rho_i$ in the magnetosheath.

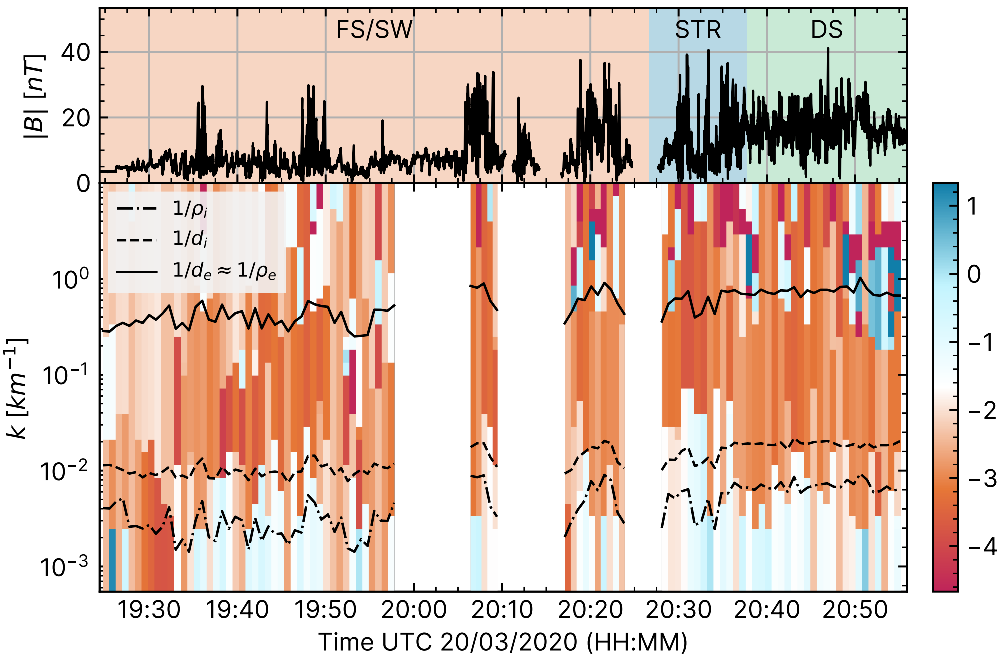

Figure 5. Equivalent to Figure 4 for interval D, 20/03/2020. The breakpoint between the MHD and ion ranges moves up from scales smaller than d_i to in-between d_i and d_e as MMS moves progressively further through the shock.

4 Kurtosis

A fundamental method for studying intermittency is to examine deviations from Gaussianity in the distribution of magnetic field fluctuations, for which a typical method is to use the kurtosis (Matthaeus et al., 2015). Intermittency is defined as strong, highly localised gradients, especially at small scales. If the kurtosis $\kappa(\boldsymbol{B}) > 3$, then the magnetic field has an overabundance of extreme gradients relative to a normal distribution, which therefore indicates the existence of intermittent structures. $\kappa \leq 3$ indicates that intermittency is not present.

Figure 7 shows the kurtosis, independent of scale, for events A and D. events B and C are shown in the supplemental material as figures S5 and S6. The kurtosis is calculated for consecutive windows containing 10^5 samples, based on the rule of thumb $p_{max} = \log N - 1$, where p_{max} is the maximum moment (i.e. fourth) and N is the number of samples (Dudok de Wit et al., 2013). In event A, we see a clear difference in kurtosis between the solar wind and magnetosheath. Intermittency is present upstream of the shock, but there are very few occasions where $\kappa > 3$ in the downstream. The kurtosis peaks to over 12 approximately $1s$ after the spacecraft crosses the shock ramp into the solar wind in event A. However, in event D, although we observe three enhancements of kurtosis above 8 which could be related to foreshock structures, similar to the enhancement to 9 in event A that precedes a slight increase in magnetic field strength, there is no clear and obvious shock transition region behaviour.

In order to directly compare the prevalence of intermittent fluctuations across the shock, we next examine the difference between the proportion of bins with $\kappa > 3$. For event A, we find that there is a large change across the shock: In the solar wind 72.4% of bins show signs of intermittency, whereas 23.1% of bins do in the magnetosheath. For

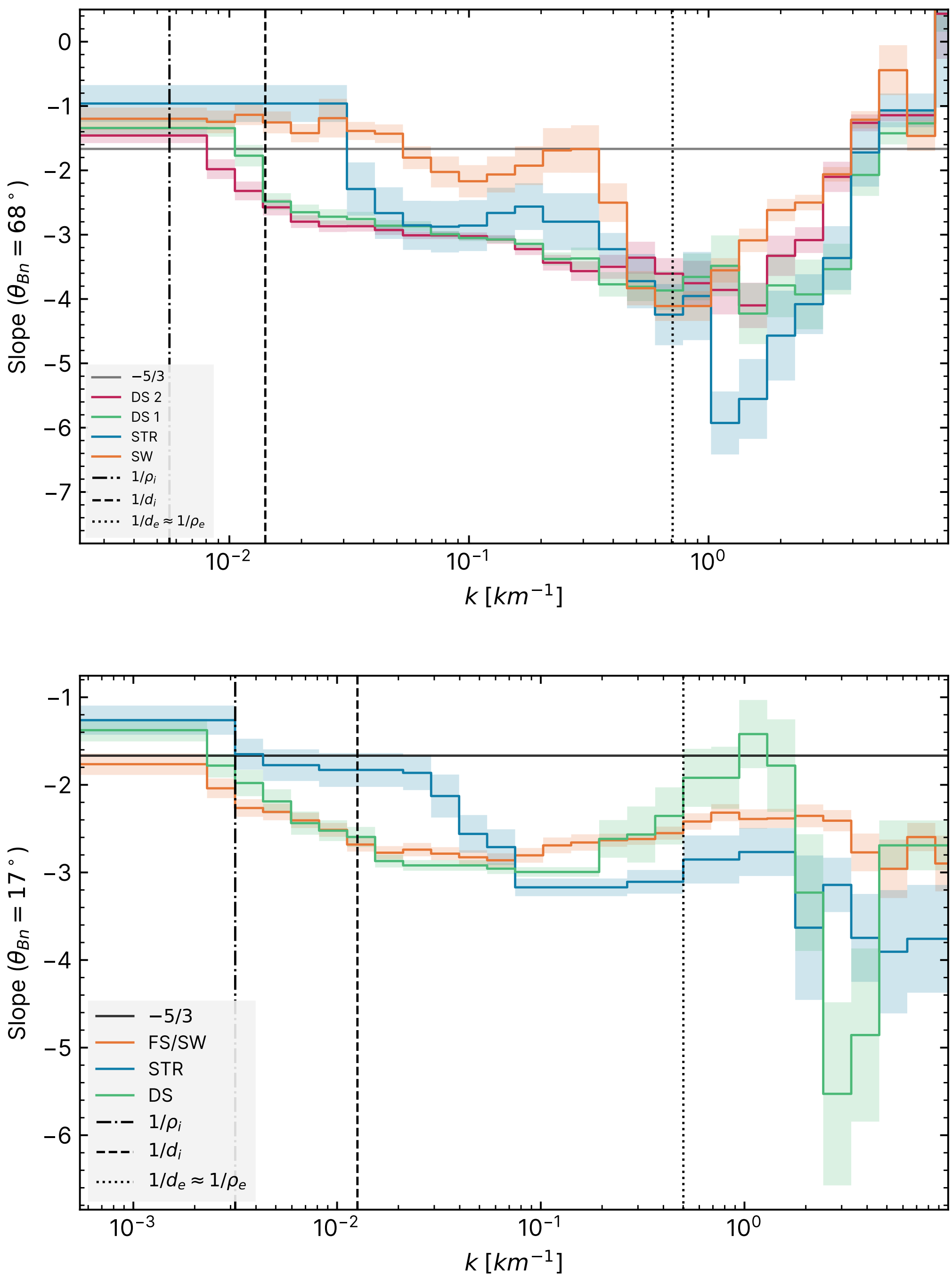

Figure 6. Average slope as a function of scale for event A (quasi-perpendicular), *top*, and event D (quasi-parallel), *bottom*. Each line represents a subsection of the entire interval, i.e. downstream (DS, red and green) of the shock, the shock transition region (STR, blue), solar wind (SW, orange), or the foreshock (FS, orange) in the case of event D where no part of the interval could be described as pure solar wind. The 'DS 2' line is further downstream than 'DS 1'. See Figures 4 and 5 for a definition of the boundaries. Kinetic scales, ρ_i d_i and d_e, are also plotted as dot-dashed, dashed and dotted vertical black lines, respectively. The Kolmogorov $-5/3$ slope is shown as a horizontal black line. There are occasions in both panels where the STR spectral index lies outside of the transition between SW and DS.

quasi parallel event D the shock is assumed to be at 20:35:26, and we observe a much lower proportion of intermittent intervals both upstream and downstream, with 22.8% in the solar wind and 17.0% in the magnetosheath. We also note that the relative reduction in the proportion of intermittent intervals from solar wind to magnetosheath is less than in the quasi-perpendicular event A.

5 Correlation Length

Next, we seek to measure the characteristic size of turbulent fluctuations in the magnetic field. Energy is typically transferred in a 'cascade' from large to small scales on average, generating magnetic structures at sizes ranging from stirring scales to the scales at which energy is dissipated. The correlation length, λ_c, quantifies the average size of the largest scale fluctuations visible in the data (Stawarz et al., 2019, 2022) which can be associated with the 'stirring' scale. Using the autocorrelation function of magnetic fluctuations, given by:

$$R(l) \equiv \frac{\langle \mathrm{Tr}[\delta \boldsymbol{b}(\boldsymbol{x}+l)\delta \boldsymbol{b}(\boldsymbol{x})] \rangle}{\langle |\delta \boldsymbol{b}|^2 \rangle}, \tag{1}$$

We define the correlation length as follows:

$$\lambda_c \equiv \int_0^\infty R(l)\, dl. \tag{2}$$

Where Tr[...] is the trace, $\delta \boldsymbol{b} \equiv \boldsymbol{B} - \langle \boldsymbol{B} \rangle$ and l is the lag of the autocorrelation. This calculation is achieved by integration up to the first zero crossing of $R(l)$, or by a fit of the form $R(l) \propto \exp(-l/\lambda_c)$. We find that results do not differ significantly between methods, and we therefore present results using the integration method.

Correlation length generally relies on having a data set long enough for a correlation function to become uncorrelated. However, the region of space near the bow shock is a rapidly changing environment dominated by processes unrelated to turbulence. Care is therefore needed when selecting what scale of fluctuations should be included. Any window of time that includes the shock will have a correlation length that is closely related to the crossing time of the shock.

In this case, it is more descriptive to examine fluctuations at scales smaller than the step-function introduced to the time series by the shock. Therefore, we use a variable high-pass filter over the event to remove the effect of low frequency variations, such as the shock ramp. A 10^{th} order Butterworth filter was used, which can be defined by the critical frequency, $F_{crit} \equiv 1/T_{max}$ where T_{max} is the longest time allowed by the filter. By varying T_{max}, the data is limited exclusively to fluctuations with wavelength shorter than $v_0/2F_{crit}$. If T_{max} is less than the period associated with the stirring scale of the turbulence, then the measured λ_c will have a dependence on the size of the filter, increasing in proportion to T_{max}. When T_{max} becomes greater than the period associated with the stirring scale, λ_c will appear to plateau, and changes in T_{max} will not have a significant effect on λ_c.

Similar to the approach used when discussing the magnetic spectrum, we have split the interval into smaller consecutive windows. The range of T_{max} was chosen to cover several decades in duration, and are approximately logarithmically spaced. The entire event is filtered according to T_{max} before being split into windows. Figure 8 describes the evolution of the frequency-dependent correlation length for event A. Plateaus - relatively large spacing between contour lines - indicate that a consistent correlation length has been reached. We see that in the solar wind, a consistent λ_c is not reached; the maximum observed correlation length is over $100d_i$. However, if MMS had continued to record

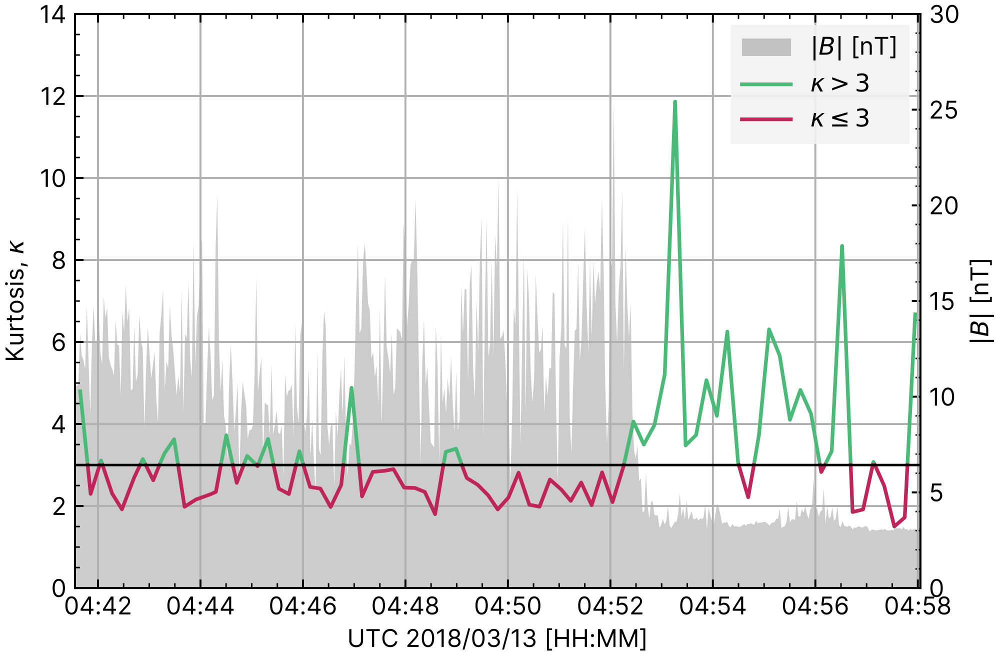

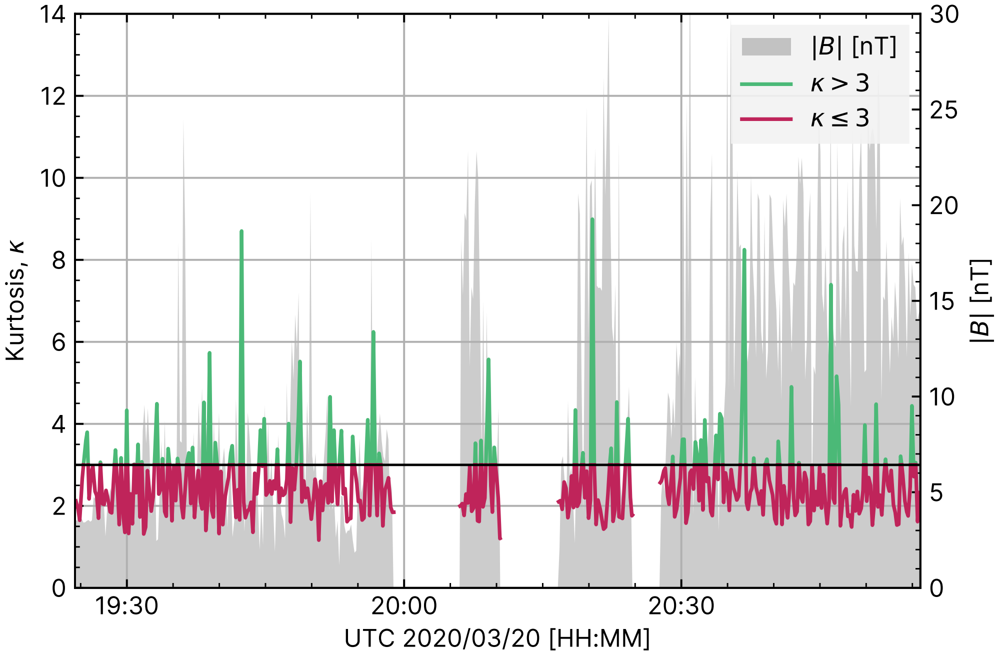

Figure 7. Kurtosis examined for events A (*top*) and D (*bottom*). $\kappa > 3$ is shown green, and $\kappa \leq 3$ is red. A horizontal black line highlights $\kappa = 3$. $|\boldsymbol{B}|$ is displayed for reference as a grey shaded background, with the vertical scale on the right. The quasi-perpendicular event A shows a clear difference between solar wind and magnetosheath, with κ peaking in the shock foot. The quasi-parallel example (event D) does not show a relationship quite as strongly, although some short periods of extreme kurtosis ($>$ 8) are present before the shock as well as a smaller spike afterwards.

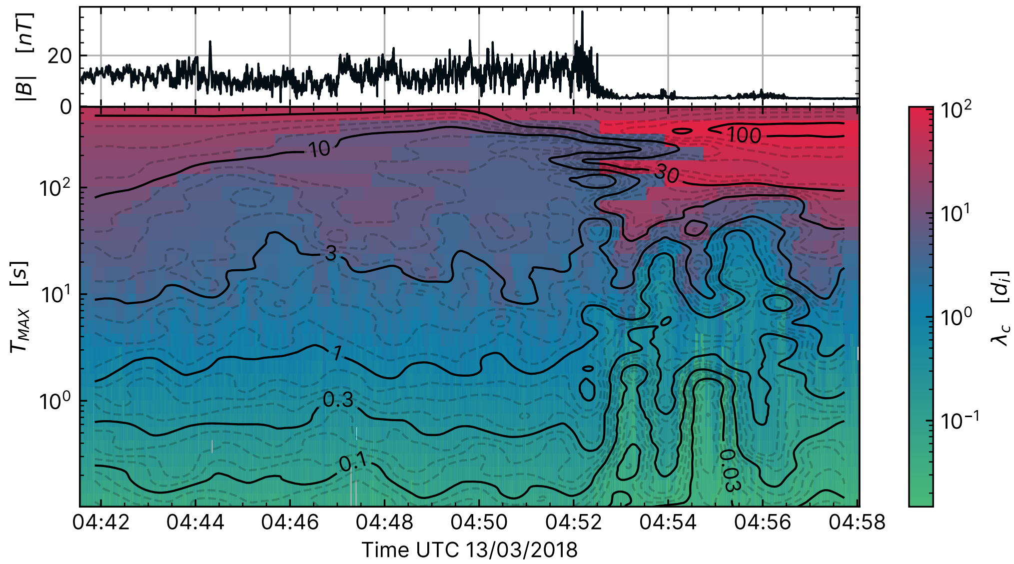

Figure 8. *Upper*: Magnetic field strength, $|B|$. *Lower*: Correlation length, λ_c, colour (units of ion inertial length), as a function of time and T_{max}. The width of each bin is equal to T_{max} up to T_{max} = total interval length/2. Contours of constant λ_c are also plotted in black. Large spacing between contour lines indicates plateaus in λ_c. A plateau indicates that the fluctuations are correlated on scales equal-to or smaller-than T_{max}. There is an observable difference in λ_c before and after the shock; a large plateau exists between the $\lambda_c = 3$ and $\lambda_c = 10$ contour lines immediately downstream of the shock, but in the region upstream of the shock transition region λ_c exceeds $100\,\mathrm{d_i}$. Contour lines were generated on a grid with a horizontal scale of 123.7 s.

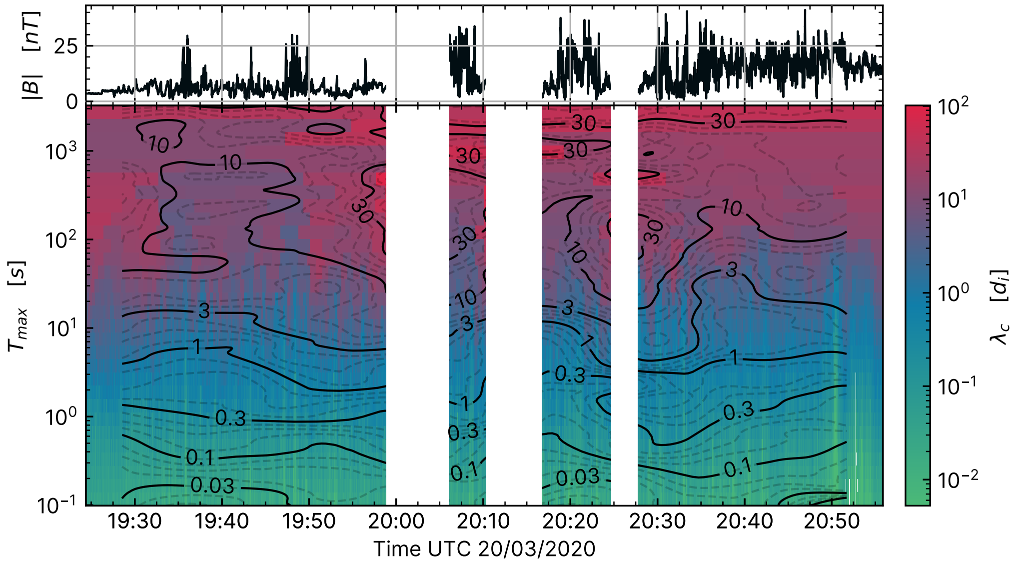

Figure 9. Similar to Figure 8 for event D. Unlike in Figure 8, there is no distinct change in correlation length across the shock easily identifiable by eye in this event. Contour lines were generated on a grid with a horizontal scale of 500 s.

data further into the solar wind we would likely have seen this increase far higher, given that solar wind correlation lengths have been measured by the ACE spacecraft at the L1 Lagrange point to be $0.03-0.08Au$, which is approximately $50-100\times10^3 d_i$ (Ragot, 2022). In the magnetosheath we see a very clear plateau of $3-10d_i$ immediately downstream of the shock, which appears to slowly increase further into the magnetosheath. At the point in the magnetosheath furthest from the shock $(04 : 42)$, the correlation length may still be in a plateau but with $\lambda_c > 10d_i$.

Figure 9 shows an equivalent plot for the quasi-parallel event, D. The correlation length on the SW side is approximately $\lambda_c = 3-10d_i$, however there are foreshock structures at 19:36, 19:48, 20:07 and 20:20, which are potential partial shock crossings, which strongly indicates that this is not representative of the solar wind, and is instead an extended shock transition region or foreshock. These structures may reduce the average correlation length, similar to Figure 8. This can be seen in the background colour but not in the contour lines, which are generated on a grid size larger than the fluctuations. The correlation length after the shock also appears to be in the range $\lambda_c = 10-30d_i$, slightly larger than what is observed for the quasi-perpendicular event A.

Figure 10 presents the same data as Figure 9 (event D), but uses $|\boldsymbol{B}|$ and $|v_{x,i}|$ as proxies for distance through the shock. Low $|\boldsymbol{B}|$ and high $|v_x|$ are associated with the solar wind, before the shock compresses and increases $|\boldsymbol{B}|$ and considerably reduces ion velocity. Therefore, high $|\boldsymbol{B}|$ and low $|v_x|$ are associated with the magnetosheath downstream of the shock. We look at the data in this way to mitigate the effects of non-stationarity and shock motion. This allows us to quantify Figures 8 and 9 more directly. We can see that the peak *observable* λ_c in the solar wind, $\lambda_c \approx 58\,\mathrm{d_i}$ is approximately halved after the shock crossing to $\lambda_c \approx 29\,\mathrm{d_i}$. As in Figures 8 and 9, we seek consistent correlation lengths λ_c that are independent of T_{max}. These are visible in Figure 10 as regions where data with high T_{max} (red crosses) are seen at similar λ_c to those with lower T_{max} (blue or green crosses). Consistent correlation lengths are observed for the solar wind at $\lambda_c \approx 25d_i$, while in the magnetosheath consistent λ_c are no higher than $20d_i$. Con-

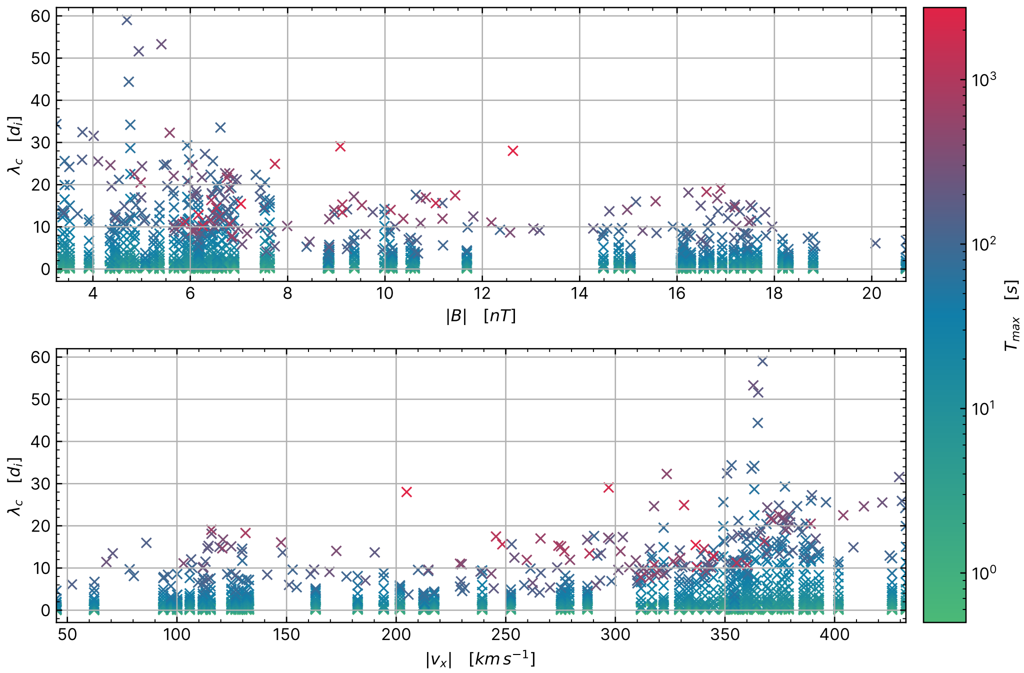

Figure 10. *Top:* λ_c against $|\boldsymbol{B}|$ for different values of T_{max} (colour) for event D. Higher $|\boldsymbol{B}|$ is correlated with distance from the shock. Three slopes fit to points of constant T_{max} are also plotted, a positive slope would correspond to λ_c increasing closer to the shock while a negative slope would be the opposite (decreasing). *Bottom:* Similar to the *top* panel, it shows λ_c against $|v_x|$ for different T_{max} (colour). Higher $|v_x|$ occurs in the solar wind before being slowed by the shock.

sistent correlation lengths are most visible in the magnetosheath where $|\boldsymbol{B}| = 17\,\mathrm{nT}$ and $|v_x| = 120\,\mathrm{km\,s^{-1}}$.

Finally, there are indications that shock micro-structure and non-stationarity may also have an effect on the correlation length. In the quasi-perpendicular case, Figure 8, we see two periods of upstream wave activity visible at 04:54 and 04:56 in the top panel, both approximately sixty seconds in duration. This causes a significant reduction of λ_c of approximately a factor of 10 compared to the immediate surroundings, but only for $T_{max} \leq 60s$. Similar structure is also visible within the shock ramp at 04:52:30. These upstream wave packets may be partial crossings of the shock foot caused by ripples on the shock surface (Johlander et al., 2016). Hence, the features in the filtered correlation length may be associated with fluctuations in the foot and ramp associated with this form of non-stationarity. A similar effect is also visible, although to a much lesser extent, in figure 9, where the periods of large amplitude magnetic field are associated with slightly lower correlation lengths than the surroundings extending to longer scales, e.g. at 19 : 35 between $T_{max} = 10$ and $T_{max} = 100$. This would seem to suggest that there are some structures in the shock transition region that can influence the stirring scales in a manner more complex than a simple transition from solar wind to magnetosheath.

6 Conclusions

In this study, we used three different measures of turbulence, the magnetic spectrum, scale-independent kurtosis and correlation length, to explore the evolution of the solar wind and magnetosheath turbulence across Earth's bow shock. The influence of the bow shock transition region on the properties of turbulence is not currently well understood. Therefore, by using the magnetic spectrum to observe differences in the turbulent energy cascade, the kurtosis to explore the properties of intermittency and the correlation length to describe changes in stirring scales, we aim to produce a representative picture of how turbulence evolves from the solar wind, across the bow shock, and downstream into the magnetosheath.

We find that the shock transition region displays features in the spacecraft frame magnetic spectrum that are different to the turbulence present in the solar wind and magnetosheath. This can be seen as shock transition spectral slopes which are steeper at multiple scales than either of their upstream or downstream neighbours (Figure 6). This suggests shock processes are driving scale dependent energy dissipation at both sub-ion and sub-electron scales. This is observed at both quasi-parallel and quasi-perpendicular shocks (events A and D, $\theta_{Bn} = 68°$ and $17°$ respectively). However, we note that these signatures are not always so clearly observable. This is the case for events B and C, which are not extensively discussed in the main body of this manuscript. Instead, figures showing structure (or lack thereof) in the magnetic spectral indices and scale-independent kurtosis are shown in the supplemental material.We find that the breakpoint (BP) separating the inertial range from the ion range transitions from $BP << d_i$ before the shock, to $d_i \leq BP \leq \rho_i$ in the magnetosheath. This occurred over a 45 s interval for event A and a 3 minute interval for event D, suggesting that the time needed for the turbulent fluctuations to transition from solar wind-like to magnetosheath-like is dependent on θ_{Bn}.

Finally, we have adapted the definition of correlation length to include a high-pass filter defined by a critical frequency F_{crit}, which allowed us to calculate a turbulent correlation length across the shock that effectively removes the large-scale spectral influence of the shock. We found that close to the shock the correlation length is longer on the solar wind side than the magnetosheath by a factor of at least 2 when considering the maximum λ_c. Plateaus in high-pass filtered correlation length averaged $25\,\mathrm{d_i}$ in the solar wind and $< 20\,\mathrm{d_i}$ in the magnetosheath. This relates to a reduction in size of the stirring scale in the magnetosheath when compared to solar wind close to the shock. We found that upstream structures in the shock transition region can affect the correlation length by introducing new plateaus for short periods of time, on the order of 10s of seconds.

We note that the case studies shown here may not be representative of all shocks. The natural next step is therefore to to determine whether the conclusions reached here are representative of the typical quasi-parallel or quasi-perpendicular shock. In a future work, we will compile a statistical survey of shocks across a range of shock normal angles and other plasma parameters, to explore the average behaviour of the bow shock.

Acknowledgments

J. Plank was supported by STFC studentship ST/V507064/1 (2502298). I. Gingell was supported by the Royal Society University Research Fellowship No. URF\R1\191547.

The data that support the findings of this study are openly available at the MMS Science Data Center at the Laboratory for Atmospheric and Space Physics (LASP) hosted by the University of Colorado, Boulder (`https://lasp.colorado.edu/mms/sdc/public/`), references (Burch et al., 2015; Ergun et al., 2014; Lindqvist et al., 2014; Torbert et al., 2014; Pollock et al., 2016), and NASA/GSFC's Space Physics Data Facility's OMNIWeb service (`https://omniweb.gsfc.nasa.gov/`, references (Lepping et al., 1995; Ogilvie et al., 1995; Smith et al., 1998; McComas et al., 1998).

References

Alexandrova, O. (2008, February). Solar wind vs magnetosheath turbulence and alfvén vortices. *Nonlinear Processes in Geophysics*, *15*(1), 95–108. Retrieved from `https://doi.org/10.5194/npg-15-95-2008` doi: 10.5194/npg-15-95-2008

Alexandrova, O., Chen, C. H. K., Sorriso-Valvo, L., Horbury, T. S., & Bale, S. D. (2013, August). Solar wind turbulence and the role of ion instabilities. *Space Science Reviews*, *178*(2-4), 101–139. Retrieved from `https://doi.org/10.1007/s11214-013-0004-8` doi: 10.1007/s11214-013-0004-8

Alexandrova, O., Saur, J., Lacombe, C., Mangeney, A., Mitchell, J., Schwartz, S. J., & Robert, P. (2009, October). Universality of solar-wind turbulent spectrum from MHD to electron scales. *Physical Review Letters*, *103*(16). Retrieved from `https://doi.org/10.1103/physrevlett.103.165003` doi: 10.1103/physrevlett.103.165003

Argall, M. R., Fischer, D., Le Contel, O., Mirioni, L., Torbert, R. B., Dors, I., ... Russell, C. T. (2018). *The fluxgate-searchcoil merged (fsm) magnetic field data product for mms.*

Bessho, N., Chen, L.-J., Stawarz, J. E., Wang, S., Hesse, M., Wilson, L. B., & Ng, J. (2022, April). Strong reconnection electric fields in shock-driven turbulence. *Physics of Plasmas*, *29*(4), 042304. Retrieved from `https://doi.org/10.1063/5.0077529` doi: 10.1063/5.0077529

Bessho, N., Chen, L.-J., Wang, S., Hesse, M., Wilson, L. B., & Ng, J. (2020, September). Magnetic reconnection and kinetic waves generated in the earth's quasi-parallel bow shock. *Physics of Plasmas*, *27*(9), 092901. Retrieved from `https://doi.org/10.1063/5.0012443` doi: 10.1063/5.0012443

Bruno, R., & Carbone, V. (2013). The solar wind as a turbulence laboratory. *Living Reviews in Solar Physics*, *10*. Retrieved from `https://doi.org/10.12942/lrsp-2013-2` doi: 10.12942/lrsp-2013-2

Burch, J. L., Moore, T. E., Torbert, R. B., & Giles, B. L. (2015, May). Magnetospheric multiscale overview and science objectives. *Space Science Reviews*, *199*(1-4), 5–21. doi: 10.1007/s11214-015-0164-9

Burch, J. L., Torbert, R. B., Phan, T. D., Chen, L.-J., Moore, T. E., Ergun, R. E., … Chandler, M. (2016, June). Electron-scale measurements of magnetic reconnection in space. *Science*, *352*(6290). Retrieved from https://doi.org/10.1126/science.aaf2939 doi: 10.1126/science.aaf2939

Carbone, V., Veltri, P., & Mangeney, A. (1990, August). Coherent structure formation and magnetic field line reconnection in magnetohydrodynamic turbulence. *Physics of Fluids A: Fluid Dynamics*, *2*(8), 1487–1496. Retrieved from https://doi.org/10.1063/1.857598 doi: 10.1063/1.857598

Chasapis, A., Matthaeus, W. H., Parashar, T. N., Wan, M., Haggerty, C. C., Pollock, C. J., … Burch, J. L. (2018, March). In situ observation of intermittent dissipation at kinetic scales in the earth's magnetosheath. *The Astrophysical Journal*, *856*(1), L19. Retrieved from https://doi.org/10.3847/2041-8213/aaadf8 doi: 10.3847/2041-8213/aaadf8

Chen, C. H. K., Leung, L., Boldyrev, S., Maruca, B. A., & Bale, S. D. (2014, November). Ion-scale spectral break of solar wind turbulence at high and low beta. *Geophysical Research Letters*, *41*(22), 8081–8088. Retrieved from https://doi.org/10.1002/2014gl062009 doi: 10.1002/2014gl062009

Contel, O. L., Leroy, P., Roux, A., Coillot, C., Alison, D., Bouabdellah, A., … de la Porte, B. (2014, September). The search-coil magnetometer for MMS. *Space Science Reviews*, *199*(1-4), 257–282. Retrieved from https://doi.org/10.1007/s11214-014-0096-9 doi: 10.1007/s11214-014-0096-9

Cranmer, S. R., Asgari-Targhi, M., Paz Miralles, M., Raymond, J. C., Strachan, L., Tian, H., & Woolsey, L. N. (2015, May). The role of turbulence in coronal heating and solar wind expansion. *Philosophical Transactions of the Royal Society A: Mathematical, Physical and Engineering Sciences*, *373*(2041), 20140148. Retrieved from https://doi.org/10.1098/rsta.2014.0148 doi: 10.1098/rsta.2014.0148

Dudok de Wit, T., Alexandrova, O., Furno, I., Sorriso-Valvo, L., & Zimbardo, G. (2013, May). Methods for characterising microphysical processes in plasmas. *Space Science Reviews*, *178*(2-4), 665–693. Retrieved from https://doi.org/10.1007/s11214-013-9974-9 doi: 10.1007/s11214-013-9974-9

Ergun, R. E., Tucker, S., Westfall, J., Goodrich, K. A., Malaspina, D. M., Summers, D., … Cully, C. M. (2014, December). The axial double probe and fields signal processing for the MMS mission. *Space Science Reviews*, *199*(1-4), 167–188. Retrieved from https://doi.org/10.1007/s11214-014-0115-x doi: 10.1007/s11214-014-0115-x

Franci, L., Cerri, S. S., Califano, F., Landi, S., Papini, E., Verdini, A., … Hellinger, P. (2017, November). Magnetic reconnection as a driver for a sub-ion-scale cascade in plasma turbulence. *The Astrophysical Journal*, *850*(1), L16. Retrieved from https://doi.org/10.3847/2041-8213/aa93fb doi: 10.3847/2041-8213/aa93fb

Franci, L., Landi, S., Matteini, L., Verdini, A., & Hellinger, P. (2015, October). HIGH-RESOLUTION HYBRID SIMULATIONS OF KINETIC PLASMA TURBULENCE AT PROTON SCALES. *The Astrophysical Journal*, *812*(1), 21. Retrieved from https://doi.org/10.1088/0004-637x/812/1/21 doi: 10.1088/0004-637x/812/1/21

Friedman, J. H. (1991, March). Multivariate adaptive regression splines. *The Annals of Statistics*, *19*(1). Retrieved from https://doi.org/10.1214/aos/1176347963 doi: 10.1214/aos/1176347963

Frisch, U. (1995). *Turbulence*. Cambridge University Press. Retrieved from https://doi.org/10.1017/cbo9781139170666 doi: 10.1017/cbo9781139170666

Gingell, I., Schwartz, S. J., Burgess, D., Johlander, A., Russell, C. T., Burch, J. L., … Wilder, F. (2017, November). MMS observations and hybrid simulations of surface ripples at a marginally quasi-parallel shock. *Jour-*

nal of Geophysical Research: Space Physics, *122*(11). Retrieved from https://doi.org/10.1002/2017ja024538 doi: 10.1002/2017ja024538

Gingell, I., Schwartz, S. J., Eastwood, J. P., Burch, J. L., Ergun, R. E., Fuselier, S., … Wilder, F. (2019, February). Observations of magnetic reconnection in the transition region of quasi-parallel shocks. *Geophysical Research Letters*, *46*(3), 1177–1184. Retrieved from https://doi.org/10.1029/2018gl081804 doi: 10.1029/2018gl081804

Hollweg, J. V. (1999, July). Kinetic alfvén wave revisited. *Journal of Geophysical Research: Space Physics*, *104*(A7), 14811–14819. Retrieved from https://doi.org/10.1029/1998ja900132 doi: 10.1029/1998ja900132

Huang, S. Y., Hadid, L. Z., Sahraoui, F., Yuan, Z. G., & Deng, X. H. (2017, February). On the existence of the kolmogorov inertial range in the terrestrial magnetosheath turbulence. *The Astrophysical Journal*, *836*(1), L10. Retrieved from https://doi.org/10.3847/2041-8213/836/1/l10 doi: 10.3847/2041-8213/836/1/l10

Isenberg, P. A., & Hollweg, J. V. (1983). On the preferential acceleration and heating of solar wind heavy ions. *Journal of Geophysical Research*, *88*(A5), 3923. Retrieved from https://doi.org/10.1029/ja088ia05p03923 doi: 10.1029/ja088ia05p03923

Johlander, A., Schwartz, S., Vaivads, A., Khotyaintsev, Y. V., Gingell, I., Peng, I., … Burch, J. (2016, October). Rippled quasiperpendicular shock observed by the magnetospheric multiscale spacecraft. *Physical Review Letters*, *117*(16). Retrieved from https://doi.org/10.1103/physrevlett.117.165101 doi: 10.1103/physrevlett.117.165101

King, J. H. (2005). Solar wind spatial scales in and comparisons of hourly wind and ACE plasma and magnetic field data. *Journal of Geophysical Research*, *110*(A2). Retrieved from https://doi.org/10.1029/2004ja010649 doi: 10.1029/2004ja010649

Kiyani, K. H., Osman, K. T., & Chapman, S. C. (2015, May). Dissipation and heating in solar wind turbulence: from the macro to the micro and back again. *Philosophical Transactions of the Royal Society A: Mathematical, Physical and Engineering Sciences*, *373*(2041), 20140155. Retrieved from https://doi.org/10.1098/rsta.2014.0155 doi: 10.1098/rsta.2014.0155

Klimchuk, J. A. (2006, March). On solving the coronal heating problem. *Solar Physics*, *234*(1), 41–77. Retrieved from https://doi.org/10.1007/s11207-006-0055-z doi: 10.1007/s11207-006-0055-z

Kolmogorov, A. (1941, January). The Local Structure of Turbulence in Incompressible Viscous Fluid for Very Large Reynolds' Numbers. *Akademiia Nauk SSSR Doklady*, *30*, 301-305.

Lepping, R. P., Acũna, M. H., Burlaga, L. F., Farrell, W. M., Slavin, J. A., Schatten, K. H., … Worley, E. M. (1995, February). The WIND magnetic field investigation. *Space Science Reviews*, *71*(1-4), 207–229. Retrieved from https://doi.org/10.1007/bf00751330 doi: 10.1007/bf00751330

Lindqvist, P.-A., Olsson, G., Torbert, R. B., King, B., Granoff, M., Rau, D., … Tucker, S. (2014, November). The spin-plane double probe electric field instrument for MMS. *Space Science Reviews*, *199*(1-4), 137–165. Retrieved from https://doi.org/10.1007/s11214-014-0116-9 doi: 10.1007/s11214-014-0116-9

Matsumoto, Y., Amano, T., Kato, T. N., & Hoshino, M. (2015, February). Stochastic electron acceleration during spontaneous turbulent reconnection in a strong shock wave. *Science*, *347*(6225), 974–978. Retrieved from https://doi.org/10.1126/science.1260168 doi: 10.1126/science.1260168

Matthaeus, W. H., Wan, M., Servidio, S., Greco, A., Osman, K. T., Oughton, S., & Dmitruk, P. (2015, May). Intermittency, nonlinear dynamics and dissipation in the solar wind and astrophysical plasmas. *Philosophical Transactions of the*

Royal Society A: Mathematical, Physical and Engineering Sciences, *373*(2041), 20140154. Retrieved from https://doi.org/10.1098/rsta.2014.0154 doi: 10.1098/rsta.2014.0154

McComas, D., Bame, S., Barker, P., Feldman, W., Phillips, J., Riley, P., & Griffee, J. (1998). *Space Science Reviews*, *86*(1/4), 563–612. Retrieved from https://doi.org/10.1023/a:1005040232597 doi: 10.1023/a:1005040232597

McKee, C. F., & Ostriker, E. C. (2007, September). Theory of star formation. *Annual Review of Astronomy and Astrophysics*, *45*(1), 565–687. Retrieved from https://doi.org/10.1146/annurev.astro.45.051806.110602 doi: 10.1146/annurev.astro.45.051806.110602

Milborrow, S., Hastie, T., & Tibshirani., R. (2011). earth: Multivariate adaptive regression splines [Computer software manual]. Retrieved from http://CRAN.R-project.org/package=earth (R package)

Ogilvie, K. W., Chornay, D. J., Fritzenreiter, R. J., Hunsaker, F., Keller, J., Lobell, J., … Gergin, E. (1995, February). SWE, a comprehensive plasma instrument for the WIND spacecraft. *Space Science Reviews*, *71*(1-4), 55–77. Retrieved from https://doi.org/10.1007/bf00751326 doi: 10.1007/bf00751326

Peredo, M., Slavin, J. A., Mazur, E., & Curtis, S. A. (1995). Three-dimensional position and shape of the bow shock and their variation with alfvénic, sonic and magnetosonic mach numbers and interplanetary magnetic field orientation. *Journal of Geophysical Research*, *100*(A5), 7907. Retrieved from https://doi.org/10.1029/94ja02545 doi: 10.1029/94ja02545

Phan, T. D., Eastwood, J. P., Shay, M. A., Drake, J. F., Sonnerup, B. U. O., Fujimoto, M., … Magnes, W. (2018, May). Electron magnetic reconnection without ion coupling in earth's turbulent magnetosheath. *Nature*, *557*(7704), 202–206. Retrieved from https://doi.org/10.1038/s41586-018-0091-5 doi: 10.1038/s41586-018-0091-5

Pollock, C., Moore, T., Jacques, A., Burch, J., Gliese, U., Saito, Y., … Zeuch, M. (2016, March). Fast plasma investigation for magnetospheric multiscale. *Space Science Reviews*, *199*(1-4), 331–406. Retrieved from https://doi.org/10.1007/s11214-016-0245-4 doi: 10.1007/s11214-016-0245-4

Ragot, B. R. (2022, March). Solar wind magnetic field correlation length: Correlation functions versus cross-field displacement diffusivity test. *The Astrophysical Journal*, *927*(2), 182. Retrieved from https://doi.org/10.3847/1538-4357/ac281b doi: 10.3847/1538-4357/ac281b

Russell, C. T., Anderson, B. J., Baumjohann, W., Bromund, K. R., Dearborn, D., Fischer, D., … Richter, I. (2014, August). The magnetospheric multiscale magnetometers. *Space Science Reviews*, *199*(1-4), 189–256. Retrieved from https://doi.org/10.1007/s11214-014-0057-3 doi: 10.1007/s11214-014-0057-3

Sahraoui, F., Goldstein, M. L., Belmont, G., Canu, P., & Rezeau, L. (2010, September). Three dimensional AnisotropickSpectra of turbulence at subproton scales in the solar wind. *Physical Review Letters*, *105*(13). Retrieved from https://doi.org/10.1103/physrevlett.105.131101 doi: 10.1103/physrevlett.105.131101

Sahraoui, F., Hadid, L., & Huang, S. (2020, February). Magnetohydrodynamic and kinetic scale turbulence in the near-earth space plasmas: a (short) biased review. *Reviews of Modern Plasma Physics*, *4*(1). Retrieved from https://doi.org/10.1007/s41614-020-0040-2 doi: 10.1007/s41614-020-0040-2

Smith, C., L'Heureux, J., Ness, N., Acuña, M., Burlaga, L., & Scheifele, J. (1998). *Space Science Reviews*, *86*(1/4), 613–632. Retrieved from https://doi.org/10.1023/a:1005092216668 doi: 10.1023/a:1005092216668

Stawarz, J. E., Eastwood, J. P., Phan, T. D., Gingell, I. L., Pyakurel, P. S., Shay, M. A., … Contel, O. L. (2022, January). Turbulence-driven magnetic reconnection and the magnetic correlation length: Observations from magnetospheric multiscale in earth's magnetosheath. *Physics of Plasmas*, *29*(1), 012302. Retrieved from `https://doi.org/10.1063/5.0071106` doi: 10.1063/5.0071106

Stawarz, J. E., Eastwood, J. P., Phan, T. D., Gingell, I. L., Shay, M. A., Burch, J. L., ... Franci, L. (2019, June). Properties of the turbulence associated with electron-only magnetic reconnection in earth's magnetosheath. *The Astrophysical Journal*, *877*(2), L37. Retrieved from `https://doi.org/10.3847/2041-8213/ab21c8` doi: 10.3847/2041-8213/ab21c8

Torbert, R. B., Russell, C. T., Magnes, W., Ergun, R. E., Lindqvist, P.-A., LeContel, O., ... Lappalainen, K. (2014, November). The FIELDS instrument suite on MMS: Scientific objectives, measurements, and data products. *Space Science Reviews*, *199*(1-4), 105–135. Retrieved from `https://doi.org/10.1007/s11214-014-0109-8` doi: 10.1007/s11214-014-0109-8

Wang, R., Lu, Q., Nakamura, R., Baumjohann, W., Russell, C. T., Burch, J. L., ... Gershman, D. (2017, October). Interaction of magnetic flux ropes via magnetic reconnection observed at the magnetopause. *Journal of Geophysical Research: Space Physics*, *122*(10), 10436–10447. Retrieved from `https://doi.org/10.1002/2017ja024482` doi: 10.1002/2017ja024482

Yordanova, E., Vörös, Z., Raptis, S., & Karlsson, T. (2020, February). Current sheet statistics in the magnetosheath. *Frontiers in Astronomy and Space Sciences*, *7*. Retrieved from `https://doi.org/10.3389/fspas.2020.00002` doi: 10.3389/fspas.2020.00002

Zhuravleva, I., Churazov, E., Schekochihin, A. A., Allen, S. W., Arévalo, P., Fabian, A. C., ... Werner, N. (2014, October). Turbulent heating in galaxy clusters brightest in x-rays. *Nature*, *515*(7525), 85–87. Retrieved from `https://doi.org/10.1038/nature13830` doi: 10.1038/nature13830

JGR: Space Physics

Supporting Information for

Intermittency at Earth's bow shock: Measures of turbulence in quasi-parallel and quasi-perpendicular shocks

J. Plank[1], I. L. Gingell[1]

[1]School of Physics and Astronomy, University of Southampton, Southampton, UK

Contents of this file

Figures S1 to S6

Introduction

The supplementary material provided here includes spectral index evolution, average spectral index, and kurtosis evolution plots for events B and C. The methods used to create the figures are identical to those used for events A and D and are documented in the 'Results' section of the manuscript.

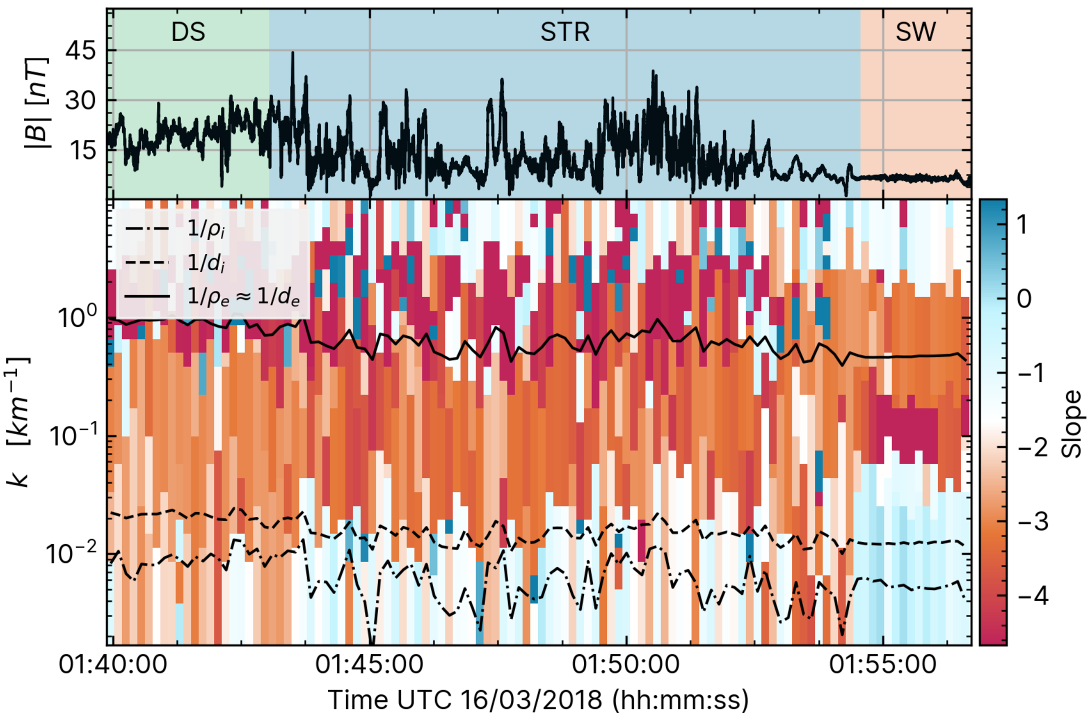

Figure S1. Evolution of spectral slopes as a function of time for event B. *Top:* Magnetic field strength, $\boldsymbol{B}$. Colours refer to downstream (DS) in green, shock transition region (STR) in blue and solar wind (SW) in orange. *Bottom:* Evolution of spectral indices from MARS fit. Note that this does not always split the spectrum into three regions. The colour represents the slope of the power-law fit. Red indicates steeper than $-5/3$, while blue is shallower than $-5/3$. Breakpoints are indicated by a change in colour. Electron scales, $\rho_e \approx d_e$ are shown as a solid black line, and ion scales d_i and ρ_i are dashed and dot-dashed black lines.

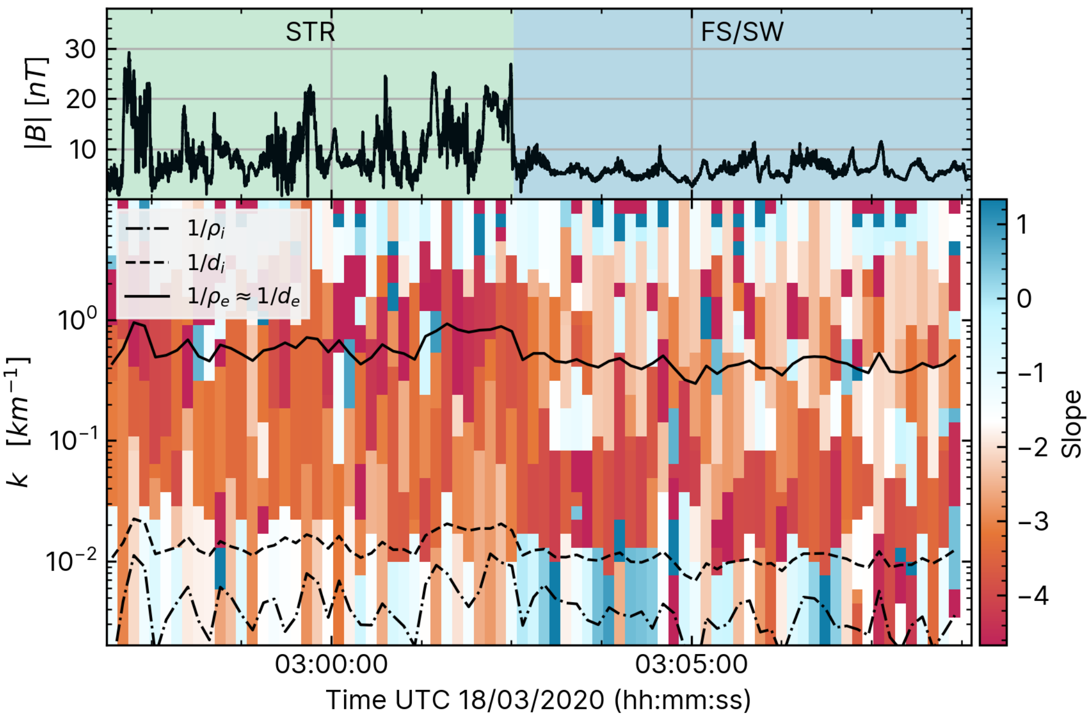

Figure S2. Evolution of spectral slopes as a function of time for event C. *Top:* Magnetic field strength, $\boldsymbol{B}$. Colours refer to shock transition region (STR) in green and foreshock/solar wind (FS/SW) in blue. *Bottom:* Evolution of spectral indices from MARS fit. Note that this does not always split the spectrum into three regions. The colour represents the slope of the power-law fit. Red indicates steeper than $-\mathbf{5/3}$, while blue is shallower than $-\mathbf{5/3}$. Breakpoints are indicated by a change in colour. Electron scales, $\boldsymbol{\rho_e} \approx \boldsymbol{d_e}$ are shown as a solid black line, and ion scales $\boldsymbol{d_i}$ and $\boldsymbol{\rho_i}$ are dashed and dot-dashed black lines.

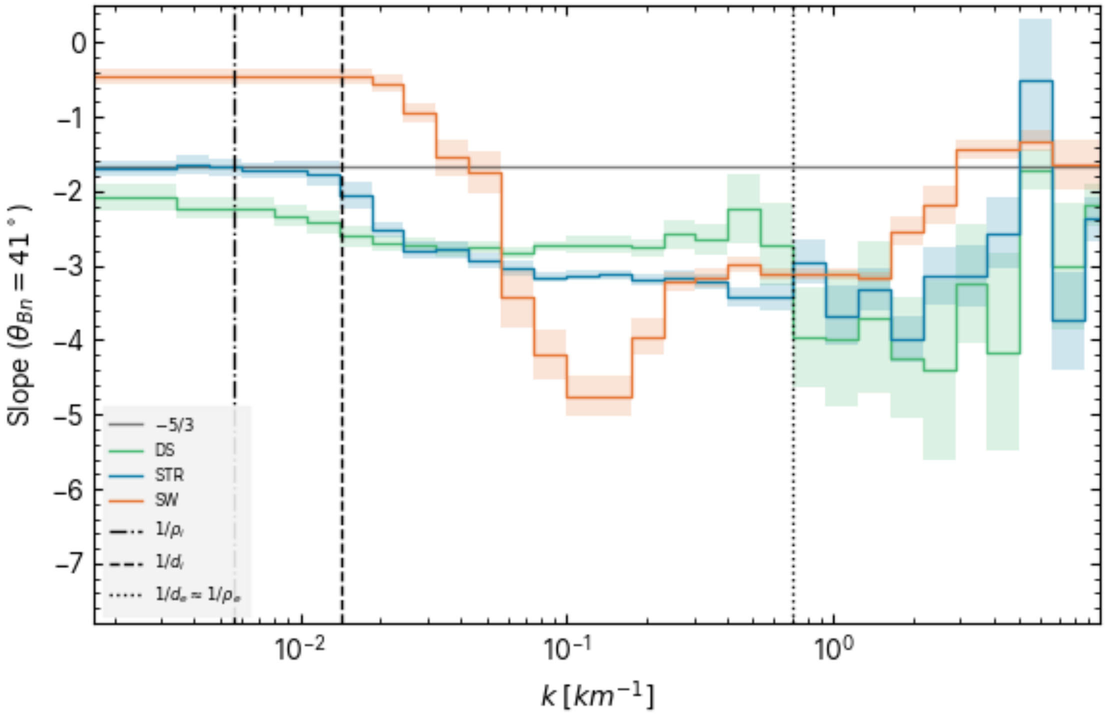

Figure S3. Average slope as a function of scale for event B. Each line represents a subsection of the entire interval. Downstream (DS) in green, shock transition region (STR) in blue, and solar wind (SW) in orange. The average ion gyroradius ρ_i and inertial length d_i are shown as dot-dashed and dashed lines respectively. The average electron gyroradius ρ_e and inertial length d_e are shown as a single dotted line. The Kolmogorov $-5/3$ slope is shown as a horizontal solid black line.

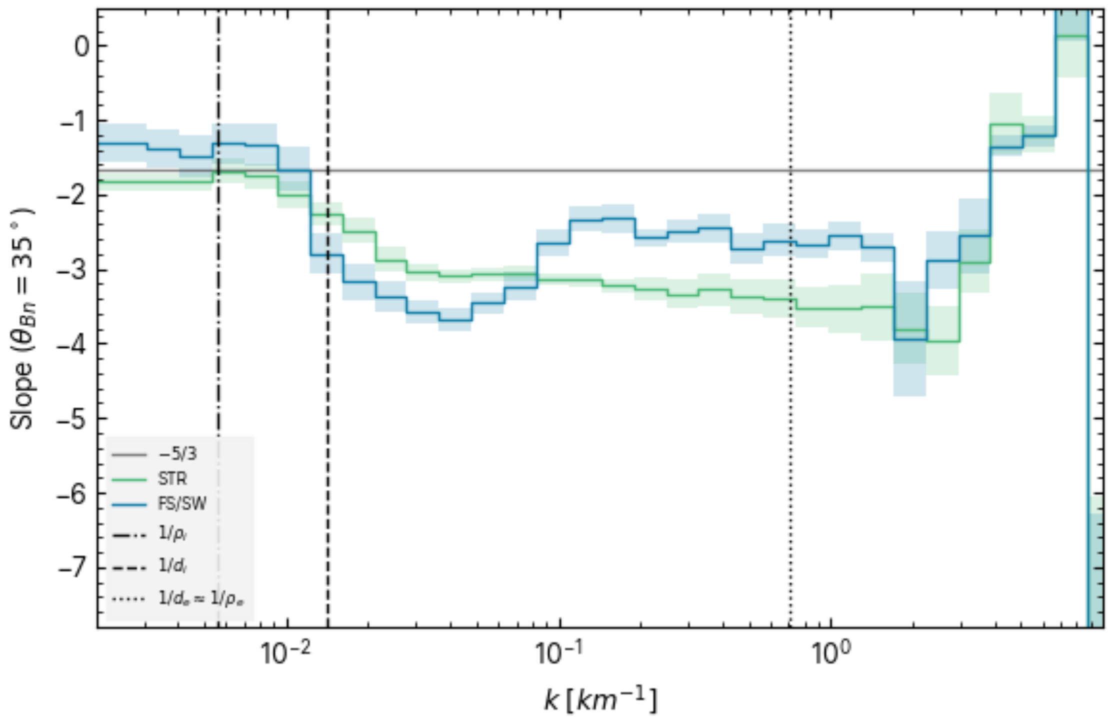

Figure S4. Average slope as a function of scale for event C. Each line represents a subsection of the entire interval. The shock transition region (STR) is shown in green, and the foreshock/solar wind (FS/SW) region is shown in blue. The average ion gyroradius ρ_i and inertial length d_i are shown as dot-dashed and dashed lines respectively. The average electron gyroradius ρ_e and inertial length d_e are shown as a single dotted line. The Kolmogorov $-5/3$ slope is shown as a horizontal solid black line.

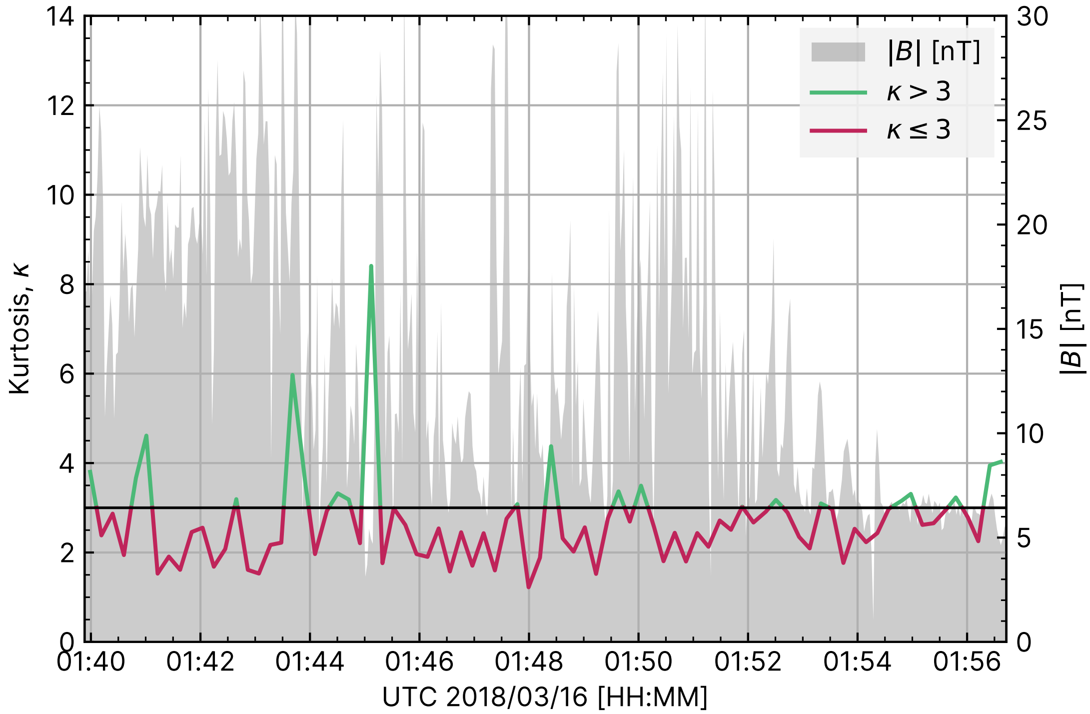

Figure S5. Kurtosis examined for event B. $\boldsymbol{\kappa} > \mathbf{3}$ is shown green, and $\boldsymbol{\kappa} \leq \mathbf{3}$ is red. A horizontal black line highlights $\boldsymbol{\kappa} = \mathbf{3}$. $|\boldsymbol{B}|$ is displayed for reference as a grey shaded background, with the vertical scale on the right.

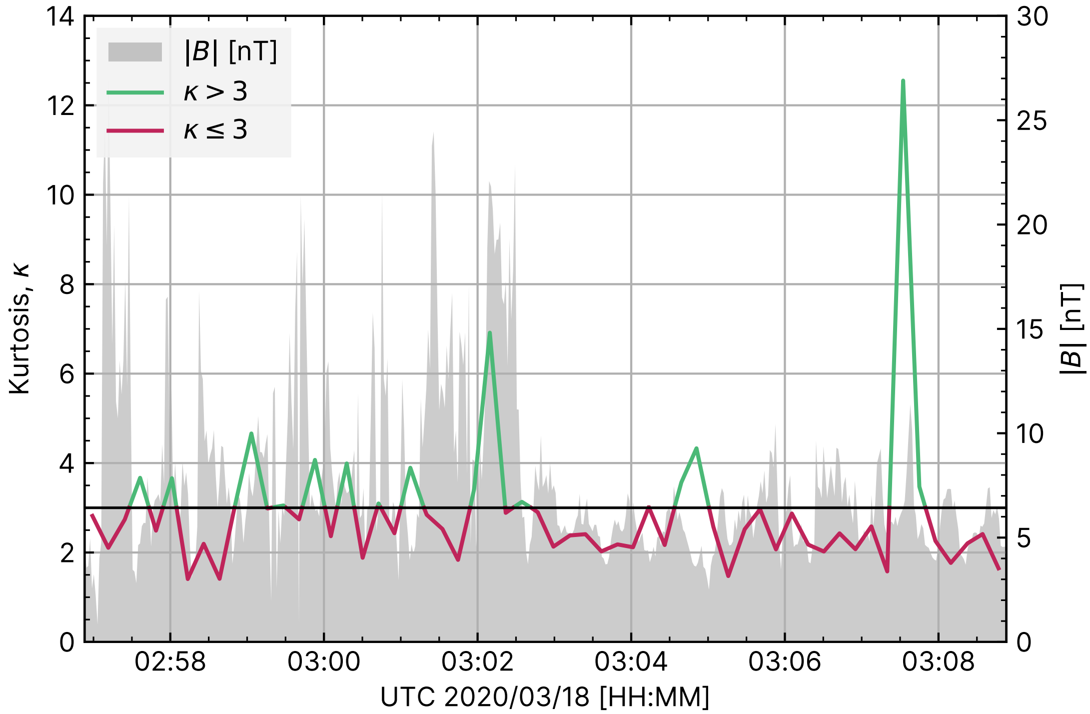

Figure S6. Kurtosis examined for event C. $\boldsymbol{\kappa > 3}$ is shown green, and $\boldsymbol{\kappa \leq 3}$ is red. A horizontal black line highlights $\boldsymbol{\kappa = 3}$. $|\boldsymbol{B}|$ is displayed for reference as a grey shaded background, with the vertical scale on the right.